Supporting Information:

Direct measurement of ballistic and diffusive electron transport in gold

Pravin Karna,[†] Md Shafkat Bin Hoque,[‡] Sandip Thakur,[†] Patrick E. Hopkins,[‡,§] and Ashutosh Giri[*,†]

†*Department of Mechanical Industrial and Systems Engineering, University of Rhode Island, Kingston, RI 02881, USA*

‡*Department of Mechanical and Aerospace Engineering, University of Virginia, Charlottesville, Virginia 22904, USA*

¶*Department of Materials Science and Engineering, University of Virginia, Charlottesville, Virginia 22904, USA*

§*Department of Physics, University of Virginia, Charlottesville, Virginia 22904, USA*

E-mail: ashgiri@uri.edu
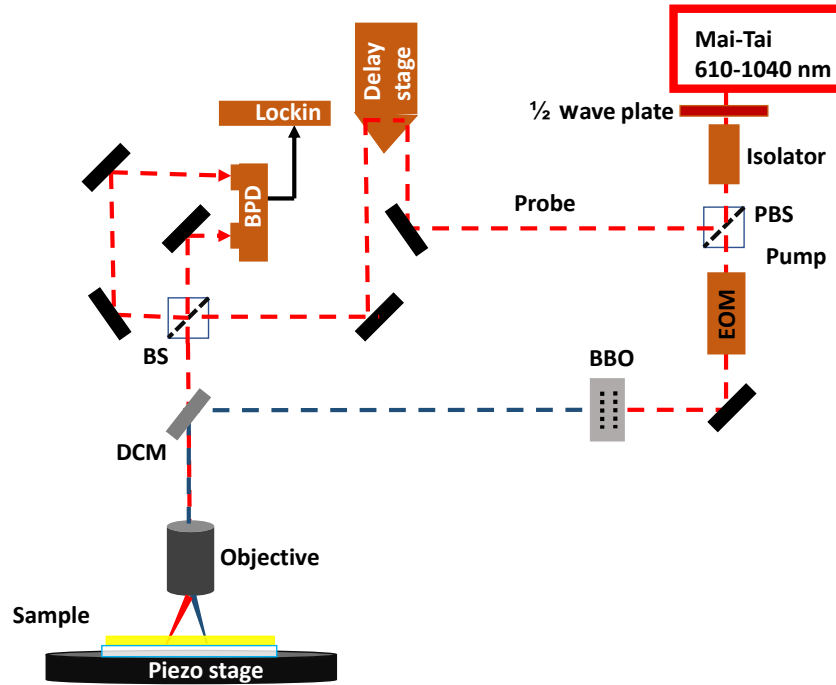
S1. Experimental Setup

Figure S1: Schematic diagram of our home-built ultrafast super-resolution thermoreflectance experimental setup.

The laser pulses emanate from a Ti:Sapphire laser with a central wavelength of 800 nm at a frequency of 80 MHz. The laser pulses are split into two paths, namely pump and probe paths using a beam splitter. An electro-optic modulator (Conoptics, 350-160-02) is used to modulate the pump beam at a repetition rate of 10 MHz. The pump beam is frequency doubled from 1.55 eV to 3.11 eV while a computer controlled mechanical delay stage (Newport M-360-90) is used to control the arrival of the probe. The probe beam is further split into a reference arm using a nonpolarising beam splitter for the balanced photodetection. The pump and the probe beams are combined using a dichroic mirror (which passes the probe but reflects the pump beam) and directed at the rear aperture of the microscope objective. Microscope objectives of 10x and 100x magnifications are used to focus the laser beams onto the sample. The probe beam is stationary throughout our measurements while the pump beam is scanned along the x-axis in both directions relative to the

stationary probe beam by moving the dichroic mirror. The mirror is mounted on a mirror mount (New Focus 8821, Newport), whose movement is controlled by a picomotor controller (New Focus Picomotor Controller/Driver, Model 8742, Newport) with nanometric resolution providing us with the ability to systematically offset the pump from the probe spot.
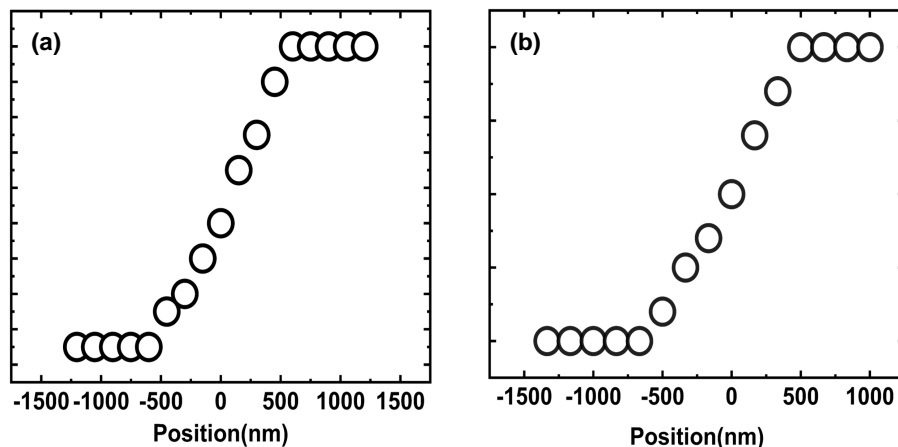

Figure S2: Knife-edge measurements of our pump and probe spot sizes with our nanometric piezostage.

The $1/e^2$ radii of the pump and probe spots with the 10x microscope objective measured using a knife-edge technique (and verified by measuring with an optical beam profiler) are ∼6.5 and 5 μm, respectively. The $1/e^2$ radii of the pump and probe spots focused on the sample using 100x are 0.65 and 0.55 μm, respectively, which is measured using knife edge measurement. The knife edge measurements are taken at a spatial resolution of 20 nm. Characteristic data from the measurements on our pump and probe spots are shown in Fig. S2.

For the knife edge measurements, a glass slide over which a thin film of gold is deposited, is used as a knife specimen. The gold thin film is used to ascertain the focal point of pump and the probe positions through the reflected image on the camera. A photodiode is placed behind the knife specimen and is connected to the oscilloscope. The piezo stage with nanometric resolution is used to accurately measure our pump and probe spot sizes. Multiple measurements are taken to ascertain the exact focal diameter of the pump and the probe.

The measurements are carried on gold thin films deposited on silicon substrates with and without an interlayer of titanium with a thickness of ~2 nm. The thickness of gold thin films are measured using optical profilometer and the measured thicknesses are in the range of 115 to 200 nm. While the pump power was adjusted between 5mW to 25 mW, the average probe power was 7
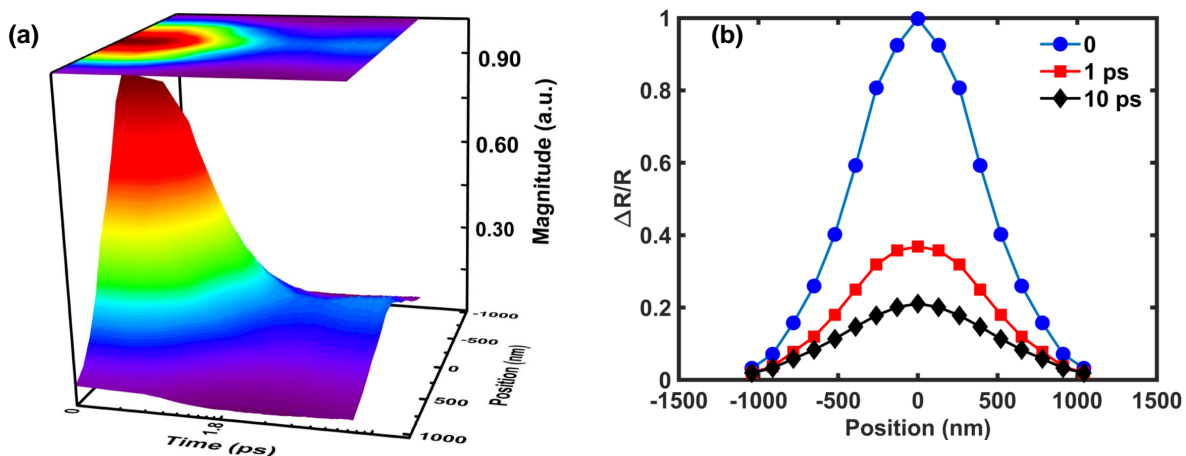

Figure S3: (a) Contour plot of the spatiotemporal decay profile of thermoreflectance signal for our gold film taken with our super-resolution thermoreflectance microscopy. (b) Thermoreflectance signals at different pump-probe time-delays as a function of our lateral pump-probe offset showing the gaussian spatial profiles.

mW for all our measurements. Note, the fluences at these laser powers are well below the ablation threshold of the gold films.[S1] We change the position of the pump beam by moving the computer-controlled dichroic scanning mirror with nanometric precision, while the probe beam is focused on a single spot. This allows us to monitor the change in thermoreflectance signal with respect to change in position of the pump spot. The reflected probe and reference signal is collected by a balance photodiode. The output of the photodiode is connected to a lockin amplifier which is locked at the pump modulation frequency. The samples are mounted over a computer-controlled 2-axis piezostage to account for nanometric control of the working distance between the objective

and the sample. Each measurement is repeated three times to calculate the uncertainties.

We plot the contour of the spatiotemporal decay of the thermoreflectance signal for our gold film in Fig. S3a. The signals obtained at various pump offsets is plotted at various pump probe delay times as shown in Fig. S3b. These $\Delta R/R$ plots provide the information about the spatial diffusion of electrons following laser excitation. We fit the data with a gaussian function to obtain the FWHM (σ) of the plots at every delay time. The σ increases with increasing pump-probe delay times. The increase in σ clearly has two distinct regimes of faster and slower into two regions as shown in Fig. 2a of the main manuscript. The general diffusion model discussed below is employed to obtain the diffusion coefficients of the electrons in these two diffusion regimes.

S2. Comparison with Au/Ti systems with varying thicknesses

A series of Au/Ti films were deposited on a sapphire substrate via electron beam evaporation at a pressure of $\sim10^{-8}$ torr. Prior to the deposition, a cleaning procedure was carried out via alcohol sonication and oxygen plasma cleaning. For our Au/Ti films, the pump-probe measurement is carried out with varying gold film thicknesses (115 nm, 150 nm and 173 nm) and varying pump and probe spot sizes as discussed below. The 2D contours in Fig. S4 (a),(b) and (c) show the spatio-temporal variation of the thermoreflectance signal obtained by varying the pump positions for pump and probe spot of $1/e^2$ radii 6.5μm and 5μm, respectively. Following laser irradiation, the hot electrons move ballistically towards the titanium layer in the cross-plane direction for these spot sizes as in-plane diffusion can not be probed at these spot sizes. Due to the stronger electron-phonon coupling of the titanium layer, the electrons scatter at the Ti layer. The titanium lattice transfers the energy back to the gold lattice as the time required by the titanium lattice to heat the substrate lattice is an order of magnitude higher.[S2] The 2D contours manifest the effect of this 'back-heating' from the titanium layer. The 'back-heating' is visibly strongest when the thickness of gold is 115 nm as seen from the 'rise' in thermoreflectance signal. As the thickness of the gold films increase, the 'back-heating' from the titanium layer is less pronounced but is still visible for

all three film thicknesses, signifying that the ballistic electrons reach the Ti layer for all thicknesses. However, with an increase in thickness of the gold thin film, the number of ballistic electrons that traverse the thickness of gold and scatter at the titanium layer decreases, and thus the 'rerise' is lower for the thicker films as compared to the 115 nm Au sample. The rise in the signal for 115, 150, 173 nm gold thin films are about 22.5%, 7.5%, and 4.4% in comparison to the lowest $\Delta R/R$ after laser excitation. We study the Au/Ti samples with a smaller pump and probe spot sizes of
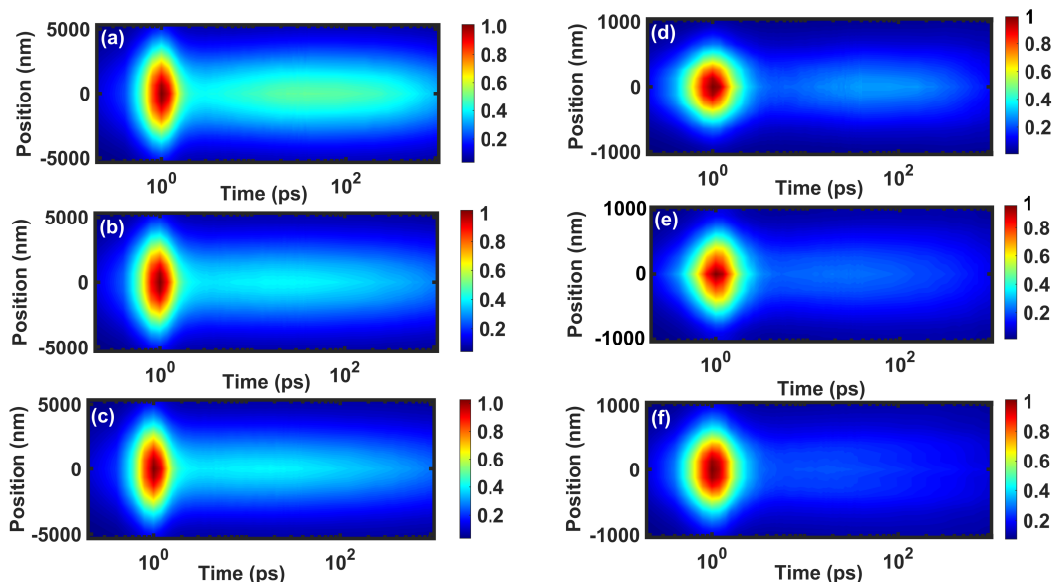

Figure S4: Contours showing the spatiotemporal variation of thermoreflectance signal taken with our $1/e^2$ pump spot radii of (i) 6.5 μm (a,b and c) and (ii) 650 nm (d,e and f) for gold thin films of thicknesses a) 115, b) 150, and c) 173 nm, respectively with a thin (2 nm) Ti adhesion layer in between the gold film and the substrate. The signature of heat flow back from the Ti layer is clearly shown by the 'rerise' of the signal in the 5 to 50 ps for all film thicknesses.

$1/e^2$ radii 0.65 μm and 0.55 μm, respectively. With these spot sizes, we will now probe both the in-plane and cross-plane diffusion since the spots are comparable to the electron diffusion lengths. The rise in temperature of the gold surface is again seen as the 'rerise' in the signal, which is prominent for our 115 nm Au sample (Fig S4d). Even though electrons escape in the in-plane direction, the 'rerise' is observable for our 150 nm gold film suggesting that the ballistic electron length is at least 150 nm.

The difference between the signals for the various films are shown in Fig. S5, where we plot

our data for the zero pump and probe offset. As is clear, the 200 nm Au film without the Ti layer has a distinctly different signal with a steady decrease in the signal from ~ 2 ps to 40 ps, whereas the Au/Ti systems show a distinct 'rerise in the signal.

We now compare the early pump-probe delay time between the Au/Ti systems and the 200 nm Au film taken with our diffraction spot sizes as shown in Fig. S6. The films with the Ti adhesion layer show a distinctly lower thermoreflectance signal at time delays of 4 ps - 10 ps signifying that the transport of electrons is characteristically different in the two cases. The lower thermoreflectance signal is indicative of reduced lattice temperature at these time regimes when the phonons have equilibrated with the electrons. This again shows that the ballistic electrons in the films with the Ti layer (including the 173 nm Au/Ti film) can scatter at the Ti layer thus changing the transport when compared to the 200 nm Au film. This supports our claim that the electron ballistic length in Au is at least 150 nm.
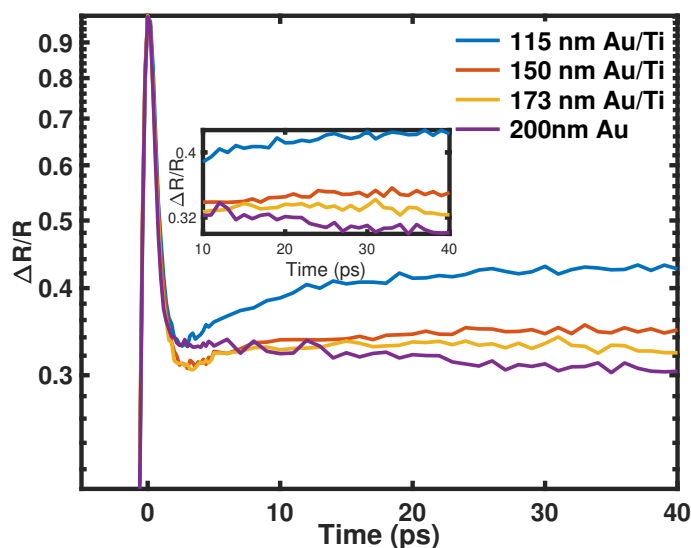

Figure S5: Variation of thermoreflectance signal for Au/Ti thin films with varying thicknesses of gold compared to our 200 Au film without the Ti adhesion layer. Clearly, the 200 nm Au film has a monotonic decrease in the thermoreflectance signal, whereas the Au/Ti systems show the 'rerise' in the signal. This suggests ballistic electrons have reached the Ti layer for all thicknesses of Au/Ti films.

When the pump beam incident on the film surface is focused to diffraction-limited spot sizes, there is considerable in-plane diffusion of the electrons. The ballistic electrons deposit their energy
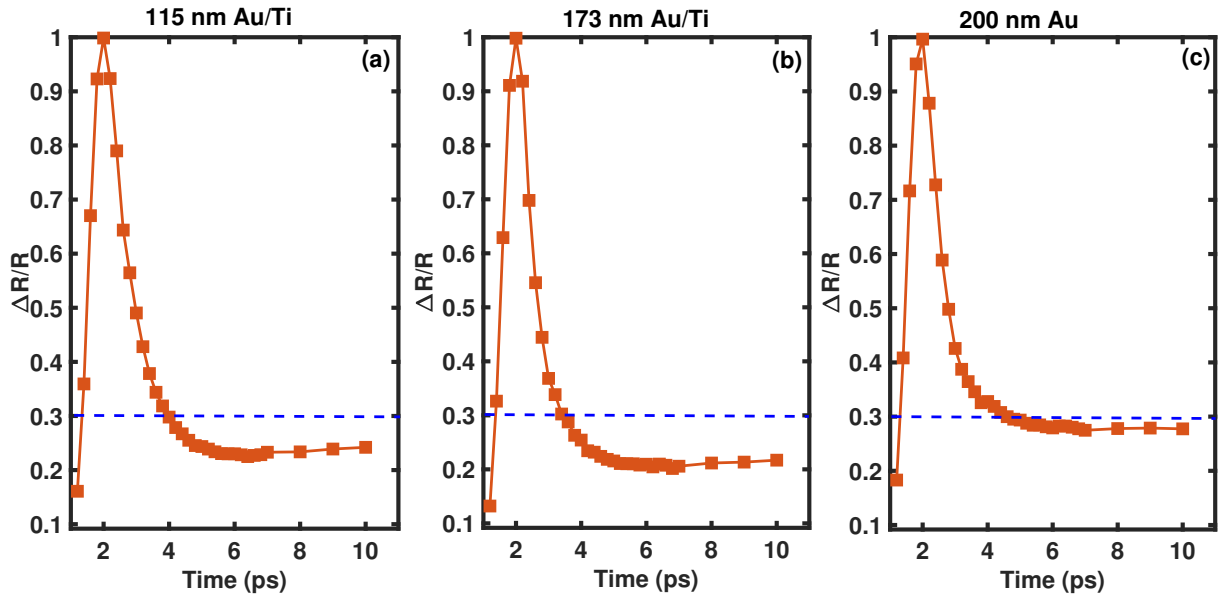
Figure S6: Comparison of thermorefelctance signal obtained for our pump spot with $1/e^2$ radius of 650 nm with concentric pump probe beam for (a) 115 nm Au/Ti (b) 173 nm Au/Ti (b) 200 nm Au. For signals when the electrons and phonons have equilibrated, the 200 nm Au sample without the Ti layer shows a relatively higher thermoreflectance signifying different transport characteristics of electrons in the Au/Ti and Au systems.
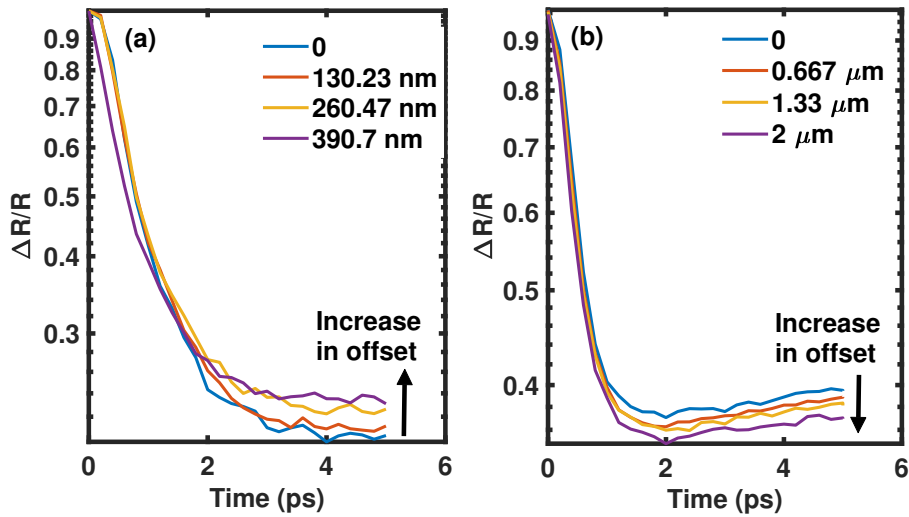

Figure S7: Comparison of thermorefelctance signals obtained for $1/e^2$ radii of pump spot size of 650 nm and 6.5 μm with non-concentric pump and probe beams. Increasing the pump-probe offset for the diffraction-limited spot size leads to an increase in the thermoreflectance signal beyond the ∼130 nm offset, which is in contrast to that for the case with the bigger spot size; the ballistic electrons deposit their energy at the ballistic length of the Au film in the lateral direction, thus increasing the lattice temperatures at those regions. This increase in temperature manifests in the higher thermoreflectance signal.

~ 200 nm as measured from our initial gaussian profile (see Fig. 1c of the main text). This causes lattice heating (after e-p coupling) at the region where these electrons deposit their energy. This manifests as higher relative thermoreflectance signal at those offsets as shown in Fig. S7a. This is not observed in the offset data with the bigger spot size as shown by the monotonically decreasing signal with offset for pump-probe delay times of >2 ps (Fig. S7b).

S3. Gaussian profiles for varying thicknesses of gold for non-thermal electrons at early pump-probe delay times

We compare the gaussian profile of the reflected probe at time delays of 400 fs, 600 fs, and 800 fs with our pump spot (of $1/e^2$ radii of 0.65 μm). We observe a signal in excess of ~ 200 nm at all time delays. This might be due to the inherent temporal resolution set by our pulse width of ~ 200 fs as well as hot electrons travelling ballistically at velocities close to the Fermi velocity.

We also compare the gaussian profiles of reflected probe at time delays of 600 fs for Au/Ti thin films with varying gold film thicknesses (115 nm, 150 nm, 173 nm) with our pump spot of $1/e^2$ radii of 0.65 μm. The gaussian profiles obtained at 600 fs after initial excitation for these films are compared with our spot size where the intensity has decreased by $1/e^2$. We observe a difference in the signal in excess of ~ 200 nm for all thicknesses. This agrees with our results for the 200 nm gold film where we also obtained an excess signal of ~ 200 nm. Therefore, the fact that there is no systematic increase in the excess signal with film thickness points to the fact that there is no noticeable out-of-plane thickness dependence on how far the electrons ballistically traverse in the in-plane direction from the excitation with the 650 nm ($1/e^2$) pump spot.

S4. General diffusion model

The diffusion coefficient or diffusivity is approximately calculated from the slope of the FWHM^2 (σ^2) versus time plot. The quantification of time dependent diffusivity $D(t)$ is carried out by
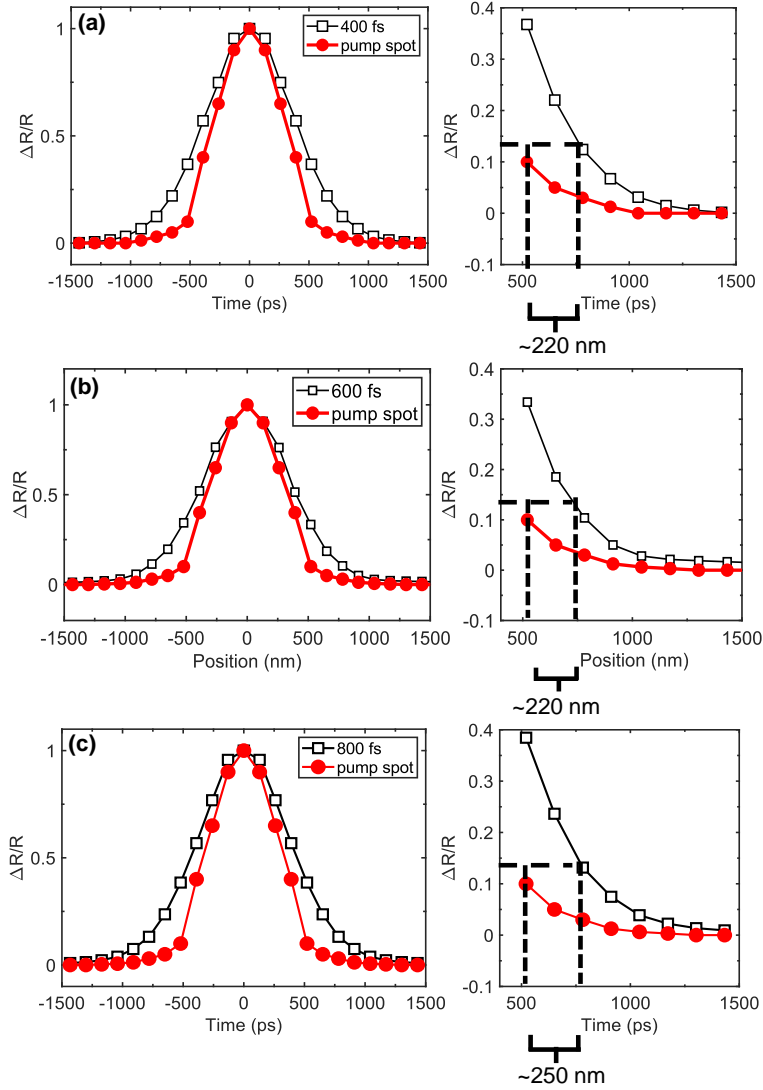
Figure S8: Comparison of gaussian profiles obtained at a) 400 fs b) 600 fs and c) 800 fs for gold thin film of thickness of 200 nm. When the gaussian profile is normalized to our pump spot size, a consistent signal in excess of ~ 200 nm is obtained at the location where the intensity has decayed by $1/e^2$, when compared to our spot size.
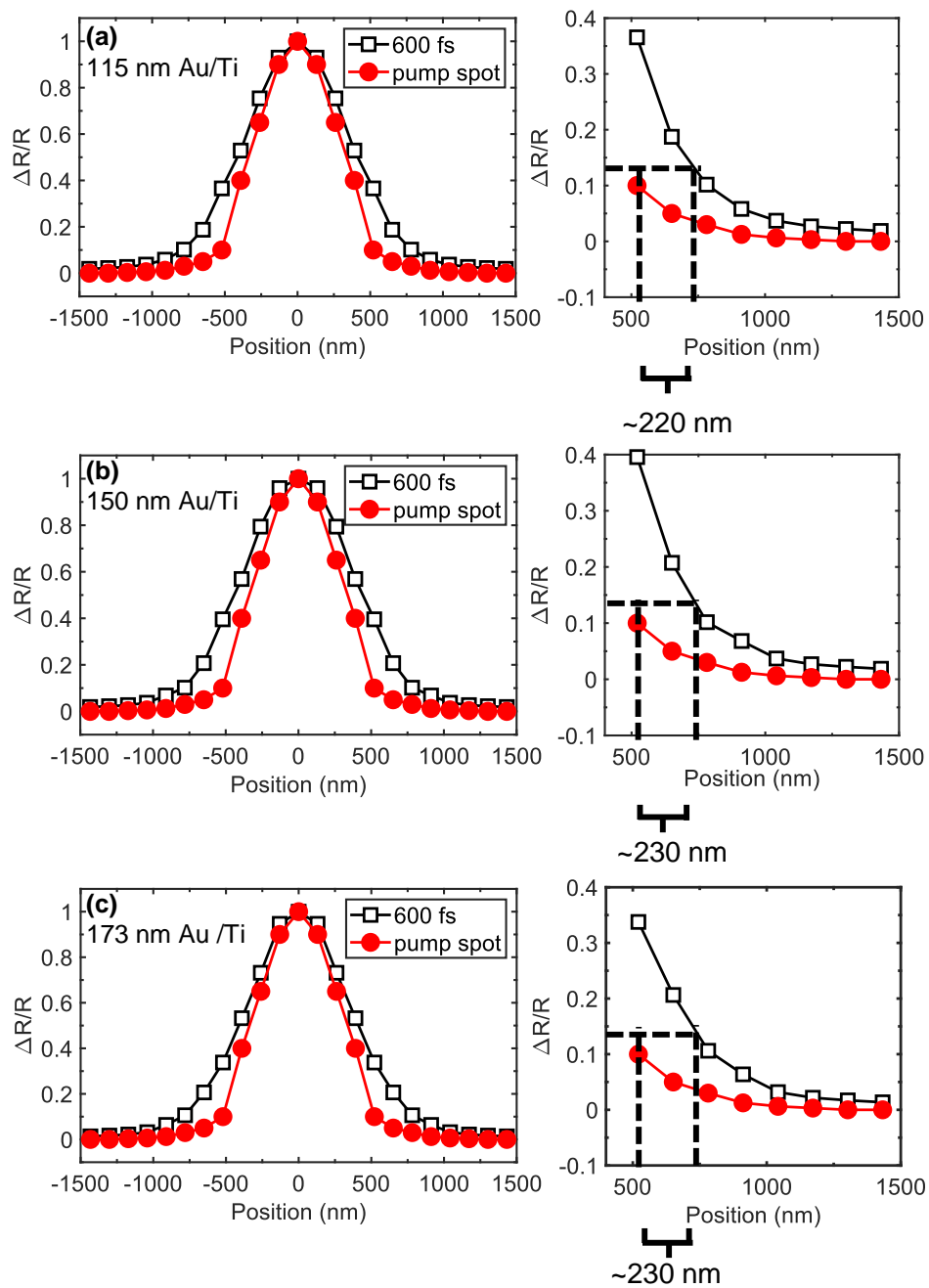
Figure S9: Comparison of gaussian profiles obtained at 600 fs for gold film of thicknesses a) 115 nm b) 150 nm and c) 173 nm with a thin intermediate Ti layer of 2 nm between the gold film and the substrate. Similar to the 200 nm gold film without the Ti adhesion layer, we observe signals in excess of $\sim$200 nm at the location where the intensity has decayed by $1/e^2$.

assuming Gaussian energy distribution due to the absorbed laser power at the sample $u(x, t = 0)$ $\propto exp(-4ln2|x^2|/\sigma_{pump}^2)$, where x$\epsilon R^n$ (n=1,2 or 3, spatial dimensions) and u evolves according to the heat diffusion equation,[S3]

$$\frac{\partial u(x,t)}{\partial t} = D(t)\nabla^2 u(x,t) \tag{1}$$

or alternatively, a heat equation with a decay rate Γ=1/τ

$$\frac{\partial u(x,t)}{\partial t} = D(t)\nabla^2 u(x,t) - \Gamma u(x,t) \tag{2}$$

The solutions for both Eq. (1) and (2) in terms of u(x,t) are gaussian in spatial profile, with a temporally decaying nature. The relation between time dependent $\sigma(t)$ and diffusivity is given by

$$\frac{\partial \sigma^2(t)}{\partial t} = 16ln2D(t) \tag{3}$$

The above equation is a generalized term for a more common time-independent diffusion coefficient D given as σ^2(t)=σ^2(0)+2Dt.

S5. Two-Temperature Model

The modified two temperature model is used to determine the dynamics of the electron and phonon temperatures following the laser excitation.[S4,S5] The time and space dependent electron temperature (T_e) and phonon temperature (T_p) are given by the coupled differential equation,

$$\begin{aligned}
C_e(T_e)\frac{\delta T_e}{\delta t} &= \nabla.(\kappa_e \nabla T_e) - G(T_e - T_p) + S(t), \\
C_p(T_p)\frac{\delta T_p}{\delta t} &= \nabla.(\kappa_p \nabla T_p) + G(T_e - T_p),
\end{aligned} \tag{4}$$

where $C_e(T_e)$=γ T_e, γ=71 J$m^{-3}K^{-2}$, γ is the Sommerfield coefficient for electron heat capacity[S6]; C_p = 2.45$\times$ 10^6 J$m^{-3}K^{-1}$ is the phonon heat capacity[S7]; κ_e=317 W m^{-1} K^{-1} is the electron
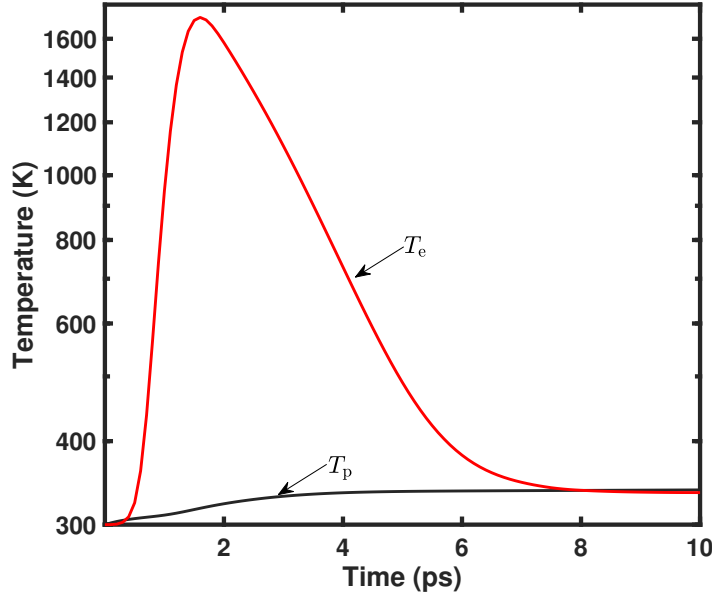
Figure S10: Transient evolution of electron and phonon temperature predicted by two temperature model at the center of the laser spot.

thermal conductivity[S6]; κ_p= 2.6 W m^{-1} K^{-1} is the phonon thermal conductivity;[S8] G=2.2$\times$ 10^{16} W m^{-3} K^{-1} is the gold electron phonon coupling coefficient.[S9] The source term in Eq.4 is given as

$$S(t) = \frac{0.94F(1-R)}{d(t_p + t_{ee})} exp\left(\frac{-2x^2}{r_0^2}\right) exp\left[-2.77\left(\frac{t - 2(t_p + t_{ee})}{t_p + t_{ee}}\right)^2\right] \tag{5}$$

here, F represents the laser fluence incident on the surface of the sample, R denotes the reflectivity of the sample, r_0 is the radius of the laser spot, d is for the film thickness, t_p denotes the width of the laser pulse and t_{ee} represents the the electron electron thermalization time. The electron-electron thermalization time is the time required for electrons after pulse absorption to relax to Fermi distribution, which is ∼600 fs.

For our laser spot sizes and fluence, the modified TTM predicts a peak electron temperature of ∼1,700 K.

S6. First Principles calculations of electron-phonon coupling

Our first-principles calculations are carried out with the Quantum Espresso package, which implements density functional perturbation theory. We use the package to determine the electron-phonon scattering rates and their coupling constants.[S10] The electrons in the Fermi surface are scattered from one particular state to another by phonons of specific modes with energy $\hbar\omega$. The possibility of this is given by Eliashberg coupling function $\alpha^2 F(\omega)$. For accurate determination of the e-p coupling, dense grids in the Brillouin zone are required to calculate the Eliashberg function, which is given as,[S11]

$$\alpha_{tr}^2 F(\omega) = \frac{1}{N(\epsilon_F)} \sum_{qj} \sum_{knm} \left| g_{k+qm,kn}^{qj} \right|^2 \delta(\hbar\omega - \hbar\omega_{qj}) \times \delta(\epsilon_{kn} - \epsilon_F)\delta(\epsilon_{k+qm} - \epsilon_F)\eta_{k+qm,kn} \quad (6)$$

where q is the phonon wave vector with branch index j, k denotes the electron wave vector, $N(\epsilon_F)$ represents the density of states (DOS) of electrons per spin at Fermi level, and $g_{k+qm,kn}^{qj}$ are the e-p matrix elements that quantify the scattering of an electron at the Fermi surface from the state $|kn\rangle$ to the state $|k+qm\rangle$. The efficiency factor,

$$\eta_{k+qm,kn} = 1 - \frac{V_k \cdot V_{k+qm}}{|V_{kn}|^2} \quad (7)$$

is dependent on the electron velocity v_{kn} and is responsible for the anisotropic behavior by taking different directions of scattering into account. It is the basic difference between the spectral function, $\alpha^2 F(\omega)$ and the transport spectral function defined in Eq.(6). The strength of e-p coupling is defined by e-p mass enhancement parameter (λ),

$$\lambda = 2 \int_0^\infty \frac{\alpha^2 F(\omega) d\omega}{\omega} \quad (8)$$

A refined k grid in the brillouin zone is a prerequisite for precise calculation of Eq. (6). The calculation is competently carried out with the Electron Phonon Wannier (EPW) package.[S12] Interpolation of the e-p matrix elements, band energies, and phonon modes is carried out from an

initial coarse grid of $18 \times 18 \times 18$ and $6 \times 6 \times 6$ to a uniform grids of $50 \times 50 \times 50$ and $35 \times 35 \times 35$, for electron (k) and phonon wave vector (q) grids, respectively by implementing maximally localized Wannier functions basis.[S13] A plane wave cutoff of 816.3 eV (60 Ry) is used for these calculations. The elevated electron temperature condition is created by smearing the Fermi Dirac distributions with $k_\mathrm{b}T_e$=3.1 eV.

For proper convergence of e-p coupling coefficient, it is necessary to ensure that the interpolated fine grids of k and q points are sufficiently dense. To check the convergence of electron and phonon wave vector grids along with the precision of Wannier representation , we confirm their localized nature by the spatial decay of Hamiltonian and the electron-phonon coupling matrix to zero. The decay of these matrices authenticates the usage of high quality interpolation. The spatial decay of these matrices for our calculations on fcc gold is given in Fig. S9.
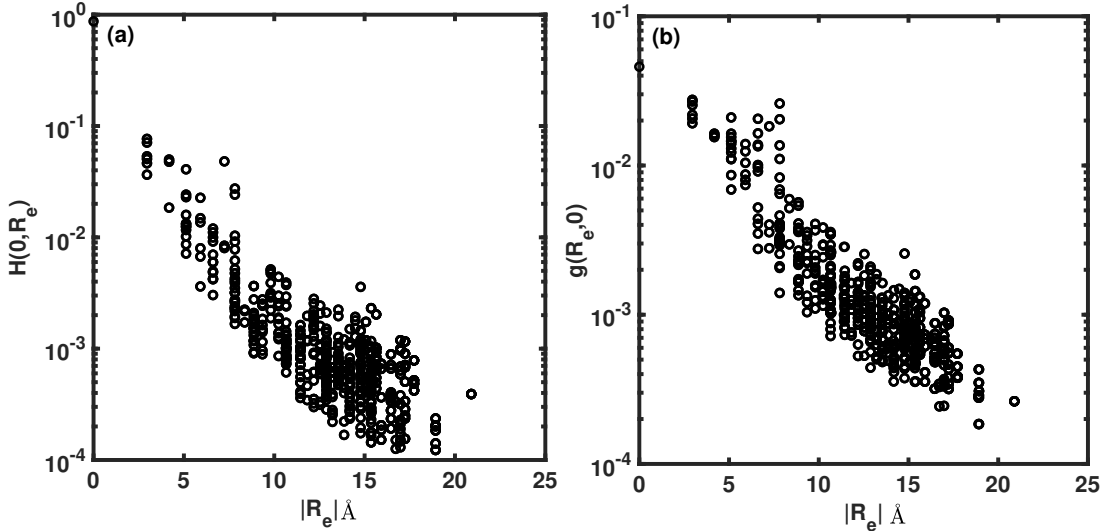

Figure S11: Spatial decay pattern of largest component of (a) the Hamiltonian and (b) the electron-phonon matrix element g(R_e,0).

The electron Hamiltonian is given as,

$$H^{el}_{R_e,R'_e} = \sum_k w_k e^{-ik\cdot(R'_e - R_e)} U^\dagger_k H^{el}_k U_k \qquad (9)$$

here w_k denotes the weight of k points, R_e represents the electron unit cell, and the transformation

between Bloch eigenstates and maximally localized Wannier functions (MLWFs)[S14,S15] is yielded by the gauge matrix U_k The electron-phonon matrix elements are given as,

$$g(R_e, R_p) = \frac{1}{N_p} \sum_{q,k} w_q e^{-i(k \cdot R_e + q \cdot R_p)} U_{k+q}^\dagger g(k,q) U_k u_q^{-1} \tag{10}$$

where U_k and U_{k+q} represent electronic matrices, u_q is representative of the phonon eigenvectors scaled by atomic masses, and the number of unit cells in the period supercell is denoted by N_p[S14,S15]. With distance, all the quantities decay to zero in the electron or phonon unit cells. The decay pattern confirms the achievement of high quality interpolation by employing maximally localized Wannier function.

References

(S1) Demaske, B. J.; Zhakhovsky, V. V.; Inogamov, N. A.; Oleynik, I. I. Ablation and spallation of gold films irradiated by ultrashort laser pulses. *Phys. Rev. B* **2010**, *82* 6, 064113.

(S2) Stoner, R.; Maris, H.; Anthony, T.; Banholzer, W. Measurements of the Kapitza conductance between diamond and several metals. *Phys. Rev. Lett.* **1992**, *68* 10, 1563.

(S3) Crank, J. *The mathematics of diffusion*; Oxford university press, 1979.

(S4) Hopkins, P. E.; Phinney, L. M.; Serrano, J. R. Re-examining electron-fermi relaxation in gold films with a nonlinear thermoreflectance model. *J Heat Transfer* **2011**, *133* 4.

(S5) Hopkins, P. E.; Duda, J. C.; Kaehr, B.; Wang Zhou, X.; Peter Yang, C.-Y.; Jones, R. E. Ultrafast and steady-state laser heating effects on electron relaxation and phonon coupling mechanisms in thin gold films. *Appl. Phys. Lett.* **2013**, *103* 21, 211910.

(S6) Bonn, M.; Denzler, D. N.; Funk, S.; Wolf, M.; Wellershoff, S.-S.; Hohlfeld, J. Ultrafast electron dynamics at metal surfaces: Competition between electron-phonon coupling and hot-electron transport. *Phys. Rev. B* **2000**, *61* 2, 1101.

(S7) Kittel, C.; McEuen, P.; McEuen, P. *Introduction to solid state physics*; Wiley New York, 1986.

(S8) Wang, Y.; Lu, Z.; Ruan, X. First principles calculation of lattice thermal conductivity of metals considering phonon-phonon and phonon-electron scattering. *J. Appl. Phys.* **2016**, *119* 22, 225109.

(S9) Lee, J. B.; Kang, K.; Lee, S. H. Comparison of theoretical models of electron-phonon coupling in thin gold films irradiated by femtosecond pulse lasers. *Mater. Trans.* **2011**, *52* 3, 547–553.

(S10) Giannozzi, P.; Baroni, S.; Bonini, N.; Calandra, M.; Car, R.; Cavazzoni, C.; Ceresoli, D.; Chiarotti, G. L.; Cococcioni, M.; Dabo, I., et al. QUANTUM ESPRESSO: a modular and open-source software project for quantum simulations of materials. *J. Phys.: Condens. Matter* **2009**, *21* 39, 395502.

(S11) Grimvall, G. The electron-phonon interaction in normal metals. *Phys. Scr.* **1976**, *14* 1 − 2, 63.

(S12) Poncé, S.; Margine, E. R.; Verdi, C.; Giustino, F. EPW: Electron–phonon coupling, transport and superconducting properties using maximally localized Wannier functions. *Comp. Phys. Commun.* **2016**, *209* 12, 116–133.

(S13) Marzari, N.; Mostofi, A. A.; Yates, J. R.; Souza, I.; Vanderbilt, D. Maximally localized Wannier functions: Theory and applications. *Rev. Mod. Phys.* **2012**, *84* 4, 1419.

(S14) Noffsinger, J. D. The Electron-Phonon Interaction from First Principles. Ph.D. thesis, UC Berkeley, 2011.

(S15) Giustino, F.; Cohen, M. L.; Louie, S. G. Electron-phonon interaction using Wannier functions. *Phys. Rev. B* **2007**, *76* 16, 165108.